Structured-light-based surface measuring for application in fluid–structure interaction

Stefan Hoerner, Cyrille Bonamy

Structured-Light Based Surface Measuring for Application in Fluid-Structure Interaction

Stefan Hoerner[1,2] & Cyrille Bonamy[2]

January 24, 2020

This article was published in the Journal:
***Experiments in Fluids* (2019) 60:168**
https://doi.org/10.1007/s00348-019-2821-3

[1]Chair of Fluid Dynamics and Technical Flows
Institute of Fluid Dynamics and Thermodynamics
Otto-von-Guericke University Magdeburg (OvGU)
Universitätsplatz 2, 39106 Magdeburg, Germany

[2]Laboratoire des Ecoulements Geophysiques et Industriels, University Grenoble Alpes, CNRS Grenoble INP*, LEGI, F-38000 Grenoble, France
*Institute of Engineering Univ. Grenoble Alpes

Corresponding author:
Stefan Hoerner, hoerner@ovgu.de

Abstract

Structured-light based profilometry techniques provide a simple and suitable tool to characterize experimentally the dynamics of the interaction between fluid and structure. The study implements a method based on the analysis of a sinusoidal fringe pattern. This method allows the retrieval of a three-dimensional surface shape from a two-dimensional video recording of the deformation of fringes projected on the surface. A detailed description of the method and the implementation is provided which will facilitate its adaption to and utilization in custom FSI applications (the code is published under open-source license). An application example is presented in the form of an experiment. A hyperflexible hydrofoil is set under forced rotational oscillation in a closed water tunnel in order to mimic the characteristics of a vertical-axis hydrokinetic cross-flow turbine. The flexible structures encounter large deformations which are linked to corresponding hydrodynamic forces. To capture this interdependence, the deformations were recorded in sync with forces registered with a six-axis load cell. A validation of the method is presented and shows good accuracy in the deformation measurements of a hyper-flexible hydrofoil. A benefit compared to other common techniques like Laser-interferometer measurements is the simplicity and modest hardware requirements of the method with the possibility to acquire height fields with good spatial and temporal resolution, which allows a spectral analysis of the surface deformation. The hydrodynamic forces are presented together with the corresponding deformation of the structure, and spectral analyses are performed which demonstrates the possibilities of the proposed method. In summary, the presented method allows the analysis of fluid-structure interactions using a simple assembly consisting of a projector and a high-speed camera. Keywords:Profilometry Surface-Tracking Fluid-Structure Interaction Hydrodynamics Flexibilty NACA0018 Pitching Foil

Nomenclature

$\Delta\phi$	phase angle shift [rad]
ϵ	$10^{-}5$ [-]
ι	imaginary number [-]
ϕ	phase angle [rad]
h	height [m]
k	wave number [m$^{-}1$]
l	length [m]
p	pivot [m]
x	position in X-axis [m]
y	position in Y-axis [m]
z	position in Z-axis [m]
α	angle of incidence [rad]
λ	wave length [m]
ρ	density [kg/m^3]
u	flow velocity [m/s]
n	number [-]
C	profile chord length [m]
D	distance between projector and zero plane [m]

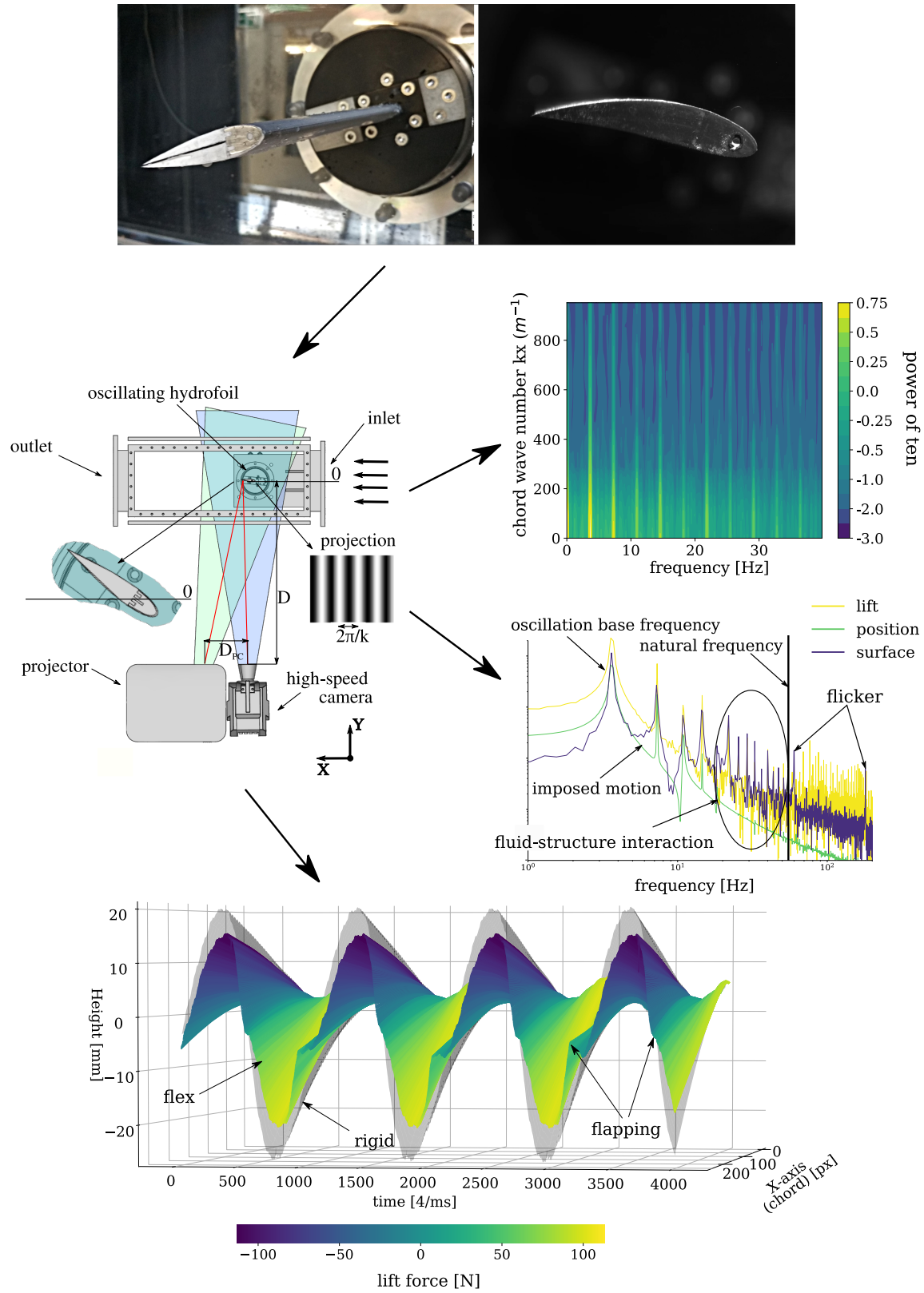

D_{PC} distance between projector and camera [m] E Young's Modulus [Pa]

F	force [N]
f	frequency [Hz]
S	surface [m^2]
T	oscillation period [-]

CFD	Computational Fluid Dynamics
CNC	Computational Numerical Control
CSM	Computational Solid Mechanics
DAC	Data Acquisition Card
FFT	Fast Fourier Transform
FSI	Fluid-Structure Interaction
h5	Hierachical Data Format v.5 (file format)
LDV	Laser-Doppler Velocimetry
PIV	Particle Image Velocimetry
Re	Reynolds number [-]
RMS	Root mean square
VTK	Vizualization Tool Kit (file format)

$'$	shifted, apparent
$_{ad}$	relative position
$_{ch}$	water channel
$_{c}$	capturing
$_{max}$	maximum
$_{pos}$	position
$_{i}$	position in X-axis on the pixel grid
$_{j}$	position in Z-axis on the pixel grid
$_{osc}$	oscillation
$_{pro}$	projected
$_{rec}$	recorded
$_{px}$	pixel
$_{q}$	position in the wave number line
$_{t}$	position in the time line of a recording

1 Introduction

Advances in available numerical codes, and foremost increases in available calculation power, are driving the research of topics with underlying fluid-structure interaction (FSI) including strong deformations of the structure. Typical applications can be found in the field of turbomachinery [11], for flying insects [14] or for medical flows [21]. Computational fluid dynamics (CFD) coupled with computational solid mechanics (CSM) produce highly-resolved, three dimensional data which can provide a better understanding of the complex mechanics. However, highly-flexible structures lead to high deformations in the fluid's spatial discretization grid, which is difficult to implement in combination with finely-resolved boundary layers for turbulent flows. Additionally, the necessary but costly two-way coupling for the large deformations makes experimental investigation methods a very interesting alternative, which may also serve for validation and calibration of numerical models.

In order to capture the characteristics of a FSI with large deformations of the structure (see Fig.1b), an experimental investigation should not only consider the flow field and the hydrodynamic forces, but also the structural response.
For the flow field, non-intrusive optical measurements methods like Laser-Doppler Velocimetry (LDV) or Particle Image Velocimetry (PIV) are the state of technology. The latter enables the measurement of an entire instantaneous field of two or three dimensions with two- or three-dimensional velocity vectors.
The hydrodynamic forces can be captured by strain gauges applied on the structure, which allow the calculation of stress and forces from the strain of the structure, or by the usage of load cells.
As for the structural deformations, a common technology is a Laser Interferometer or a Laser-Doppler Vibrometer. These sensors are part of many studies concerning FSI, e.g. Astolfi et al 2015 [1], Ducoin et al 2012 [4], Pärsinnen et al 2007 [15] or Naik et al 2003 [13]. They can track the distance to a surface with high precision and temporal resolution, are non-intrusive, and easy to handle because they do not require any post-processing steps. But the results are comparable to those from LDV measurements for fluid flows which only measure at one single point.

Rojratsirikul et al 2009 measured a cut section of a membrane wing using a Laser sheet for illumination and a video camera to capture it. They were

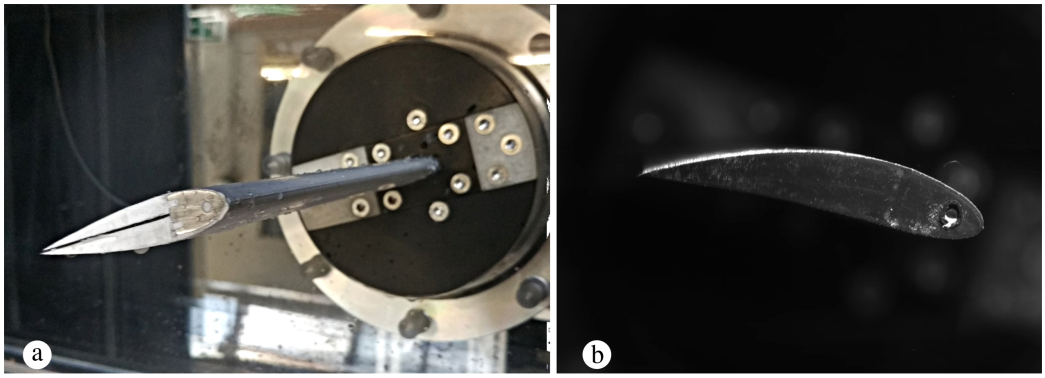

Figure 1: (a) The symmetric composite hydrofoil (NACA0018) mounted in the LEGI water tunnel. (b) The hydrofoil encounters large deformations at high angles of incidence [7].

able to perform spectral analysis and to find spatial modes in the longitudinal but not in the transversal direction of the membrane [17].

A time-resolved measurement of a whole surface provides a wealth of information about the characteristics of the structural response, much like PIV measurements do about the flow in fluid dynamics. A study with acquisition of the instantaneous deformation field was presented by Tregidgo et al 2013 [19]. Their investigations of the FSI on a pitching membrane wing included digital image correlation measurements based on two cameras to achieve stereographic view of the wing. The time-resolved acquisition of the instantaneous deformations of the surface allowed to characterize the transient effects on the membrane after the pitch motion stopped.

Structured-light based surface measurements also allow such instantaneous measurement of the entire surface. These methods are very common, well documented and also widely used in particular for medical applications, industrial surface quality control or face recognition tasks. A detailed overview of the state of the technology with focus on shape recognition is given by Zhang 2010 [22]. In this method, a pattern is projected on a surface and subsequently recorded by a single high-speed camera. When the light is projected on a non-uniform shape, the pattern is deformed in the image, and information about the surface height can be obtained.

Van der Jeught et al [20] distinguish different methods of structured-light based profilometry, according to the color mode, the pattern, the analysis and the acquisition method. A variety of methods have been developed and adapted to specific application fields. Common applications of these methods in fluid dynamics are the classification of fluid films or the acquisition of the droplet shapes. Li et al studied the dynamics of water droplet impacts using structured-light based profilometry [9]. The spatial resolution of the recordings was estimated to be 0.015 mm. The droplets were captured with 5000 fps, which allowed a characterization of the shape changes of the droplets during impact with a high precision and temporal resolution. Hassaini et al studied wave turbulence with profilometry techniques, with tracking of the air-water interface of a free-surface flow [5]. Their *MATLAB* based code, which delivered time-resolved wave motion, was used as a starting point for the development presented in this study and used for a first evaluation of the capabilities of the method to track large deformations in FSI.

In this study, the distance from a surface to the camera-projector couple is determined by measuring the shift of the phase angle of the projected fringes (see Fig.2). The comparison with the undistorted pattern obtained from a flat reference surface provides knowledge of the reference phase angle and allows to retrieve the deformation. An advantage over stereoscopic methods is that a three-dimensional surface can be tracked with a two-dimensional video recording, if the motion is of an out-of-plane character. The measurement of a linear, in-plane motion, which does not include a profile change, requires further code adaptations and might be better measured with more sophisticated methods.

These non-intrusive methods cannot reach the accuracy of a contact-based profilometry using a mechanical probe-based contour measurement method. They are also prone to reflections from polished surfaces (though an effort has been made in the scientific community to overcome this drawback using high-dynamic range techniques

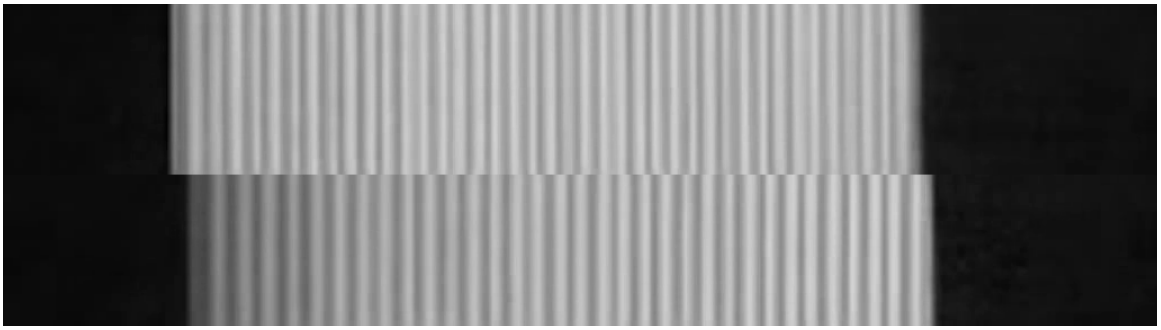

Figure 2: SFT fringe pattern detail of two arbitrary frames of a recording of the rigid hydrofoil. The fringe deformation of the pattern is visible as well as the changes in the apparent surface length, the latter is a result of the two dimensional camera view and the three dimensional oscillation and deformation. The black areas are regions without a surface and so without projection, which irritate the processing algorithm.

as reported by Lin et al 2017 [10]). However, those methods are relatively simple, rapidly implemented, and require equipment which are nowadays part of the standard instrumentation for fluid dynamics laboratories.

A high-speed surface tracking method applied on a FSI case with hyper flexible structures which display large deformations (see Fig. 1) will be presented. The code was implemented in the existing Python framework *fluidimage*, a toolbox for experiments in fluid mechanics [2, 3] published under CeCILL-B, in order to enable the utilization of the code in custom FSI projects. The toolbox takes advantage of existing strategies for massively parallel processing. An effort was made to implement the code in an effective manner in order to provide good scalability, fast processing and to allow easy adaptation to specific requirements. In the following sections, a general description of the methodology and its custom implementation and adaption to the application on FSI is given. Subsequently, the experimental setup of an example case is described, followed by a calibration and error determination section. Finally the results and the potentials of the method are presented and discussed based on the example.

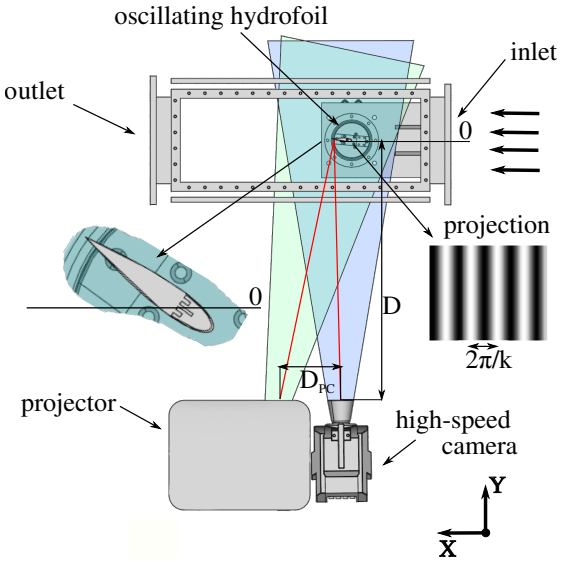

Figure 3: Setup of the experimental example case. A NACA0018 hydrofoil is set under forced pitch motion in a closed water tunnel. The sinusoidal fringe patterns are projected and captured from underneath the control section.

2 Methodology

The methodology proposed is based on a fringe pattern analysis of structured light projected on a surface. An implementation of the method presented by Takeda et al 1983 [18] is realized. To this effect, a structured grey-scale light pattern of a sine function with wave length $\lambda_{pro} = 2\pi/k_{pro}$ is projected on a white surface. This is achieved through

a projector installed perpendicular to the structure (see Fig. 2 for a typical fringe pattern). k_{pro} is the wave number from the projector. The wave length is chosen with consideration for the resolution of the projector and the projection plane. The projection is subsequently recorded by a high-speed camera which is placed in parallel to the projector (see Fig. 3). The recording will result in a different wave length than projected. This is caused by projector/camera resolution and projection magnification. The wave length of the recording, λ_{rec}, has to be determined during initialization, before the processing of the videos starts. A planar, in-plane reference surface is used to determine the length of the projected wave number and serves as the height reference for subsequent recordings, in order to remove lens distortion and aberrations.

The experimental setup leads the projector beam through the different materials (see Fig.3&4). According to the Snell-Descartes law, the beam will be refracted while it passes each of the material boundaries. This leads to a magnified apparent distance D'. This apparent object distance D'=1.15 m is calculated using the given geometrical parameters and the refraction indexes of the materials (air = 1.00029, polyacrylic = 1.4899 and water = 1.3333). The distance in between projector and camera appears to be smaller because the refracted angle ϕ' appears to be steeper (red dashed line in Fig.4). From the intercept theorem, the apparent distance between projector and camera is obtained as D'_{PC}=0.28 m.

Any deformation of the structure results in a change of the distance from the structure to the projector and will lead to a change of the projected pattern caused by a local defocussing of the projection. This will result in a new phase angle ϕ'. The phase angle shift $\Delta\phi_{i,j,t}$ is calculated for each pixel with coordinates (i,j) at each time step t/f_{c} with:

$$\Delta\phi_{i,j,t} = \phi'_{i,j,t} - \phi_{i,j,t_0} \tag{1}$$

where ϕ_{i,j,t_0} is the original phase recorded by the camera. After unwrapping the phase angle and calculating the phase shift, the surface height can be extracted with

$$h_{i,j,t} = \frac{D' \cdot \Delta\phi_{i,j,t}}{\Delta\phi_{i,j,t} - \frac{2\pi}{\lambda_{\text{rec}}} \cdot D'_{\text{PC}}} \tag{2}$$

where λ_{rec} is the recorded wave length, D' is the apparent distance, and D'_{PC} is the apparent distance between projector and camera. Maurel et al 2009 [12] determine a coordinate shift in dependence to the surface height. However the correction proposed,

$$x_{i,j,t} = \frac{x'_{i,j,t}}{1 - \frac{h_{i,j,t}}{D'}} \tag{3}$$

(here displayed with notation adapted to the present case; $x'_{i,j,t}$ and $x_{i,j,t}$ being respectively the apparent and real position in X-axis corresponding to the measured height $h_{i,j,t}$), is time-intensive.

At its maximum, with $h_{\max}$=0.02475 m, D'=1.15 m, and $x'_{\max}$=0.066 m, the shift is about $\delta x_{i,j,t\max}$=1.3 mm which is about 2% of the total width. Given this relatively minor aberration and the fact that the matrix containing the surface height is resized at pixel level and projected on a standardized pixel grid - as described subsequently - a detailed calculation of this coordinate deviation can be considered to be negligible in the application presented and, as a consequence, was not performed for the given setup. However, this systematic error is found in the results presented in section 5.

Since the recording is in two dimensions, the apparent profile length changes as a function of the profile inclination ($C' = C \cdot \cos\alpha$, see Fig.5). This will result in a shift of the apparent coordinate, since the recording is in fixed reference frame while the foil moves. In the current application this will generate further challenges.

The method cannot deal with areas where the fringe is not projected. These appear as a black band of huge range and disturb the Fast-Fourier-Transform (FFT) algorithm, performed in the later processing stage of the method (see Fig.2 for a sample of the recording for two different inclination angles). A segmentation algorithm tracks the area containing the hydrofoil, and crops the image accordingly; as a result, the size of the matrix varies with time. To be able to process these varying image details, they are inserted in an image matrix of the reference surface with the size of the non-inclined hydrofoil. This will replace the black areas by the undistorted fringe pattern. After processing, the surface area results are cropped again and then mapped on a fixed size lattice with resizing of the matrix with a spline interpolation function of first order (see Fig.5). The physical length can be found by multiplication of the pixel grid with the pixel size and the cosine of the inclination angle:

$$l = l_{\text{px}} \cdot px_{\text{size}} \cdot \cos(\alpha) \tag{4}$$

Despite the changing length of the hydrofoil, the number of pixels of the stored matrix containing

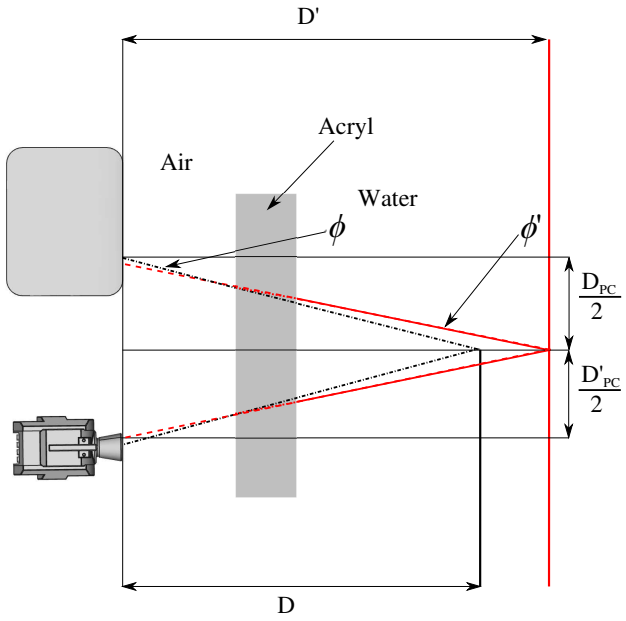

Figure 4: Magnification from refraction: The differences in the refraction index of the materials lead to an apparent magnified distance from the object to the camera and has to be taken into account for the surface tracking measurement. This is also true for the distance in between projector and camera which appears to be smaller as a consequence of the refracted angles.

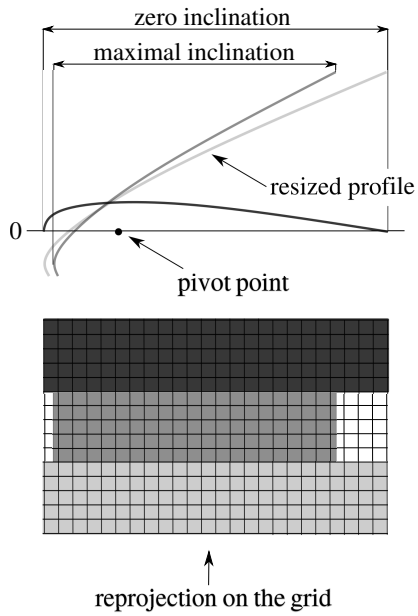

Figure 5: The two-dimensional recording leads to a change of the projected length perpendicular to the rotation axis. A resizing and reprojecting to a grid of the length of zero inclination simplifies to process and visualize the data.

the surface height remains the same, and is equal to the image matrix of the zero inclination angle. These pre- and post-processing steps simplify the signal processing and also further analysis of the data in particular for time based investigations. The practical implementation of the method includes further steps:

- For the initialization, the wave length of the recording λ_{rec} has to be determined. It is calculated using the maximum peak frequency f_{max} of a FFT over several frames, the recorded pixel length l_{px} and the number of pixels in the direction of the wave propagation n_{px} of the recording:

$$\lambda_{\mathrm{rec}} = \frac{n_{\mathrm{px}}}{f_{\mathrm{max}} \cdot l_{\mathrm{px}}} \tag{5}$$

- The processing of each frame of the high-speed video begins with a detection of the structure and the cropping of the image with a simple segmentation function;

- The second step consists of normalizing the frame by subtraction of the frame's average from itself to generate a value range from -1 to 1; amplifying with a gain of $e^{-i \cdot k_{\mathrm{rec}} \cdot x}$ and subsequent filtering with a band pass close to the wave number k_{rec} in the Fourier space to remove noise;

- The phase angle is retrieved from the complex function and subsequently unwrapped;

- A spatial 2π discontinuity detection and correction is performed to obtain a continuous surface;

- The surface height is extracted by application of Eq.2;

- A temporal discontinuity detection and correction is conducted as well in order to remove 2π jumps in time (in contrast to the method of Takeda et al [18] where this was not performed);

- The result is stored in h5 containers to allow an easy and direct access to the data.

Finally, a wrapper function allows to transform the surface data in VTK format and to visualize the data in the open-source toolkit *Paraview*, where the data can also be further post-processed. Additional Python utilities related to the following example case are also published and available under GPLv3 [6].

Table 1: Experimental setup

Oscillation frequency	f_{osc}	[Hz]	3.66
Channel flow speed	u_{ch}	[m/s]	3
Profile chord length	C	[m]	0.066
Reynolds number	Re	[-]	200,000

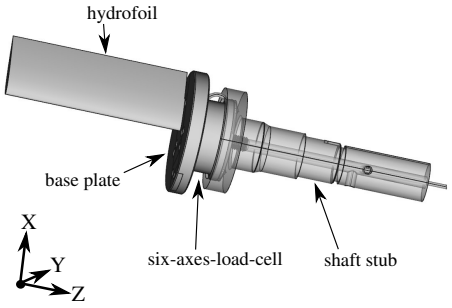

Figure 6: Placement of the sensor in between the transmission shaft stub and the hydrofoil. The origin of the coordinate system is the rotation center of the shaft at the upper side of the mounting plate, which is in one plane with tunnel section wall.

3 Oscillating hydrofoil example case

The method is applied on a FSI case consisting of a pitching, hyperflexible, composite hydrofoil mounted in a closed water tunnel. The symmetric NACA0018 profile will encounter large deformations of up to 20% of its chord length (see Fig.1&3). For reference and to calibrate the method the experiment is repeated for a hydrofoil milled from aluminum under the same conditions as before. This hydrofoil is considered to be rigid in the sense that the expected deformations will lie below the measurement uncertainty of the method. The parameters of the experimental setup are summarized in Tab.1.

The hydrofoils follow a non-sinusoidal oscillation trajectory. The trajectory of the inclination angle is comparable to the angle of incidence of a blade in a vertical-axis hydrokinetic turbine. The experimental setup mimics the flow characteristics of such a turbine at blade level to investigate the FSI for a runner with highly flexible blades (see [7] for details). The average oscillation frequency is f_{osc}=3.66 Hz and the maximum angle of incidence is α=30° for the hydrofoil motion. The shape of the trajectory is given with respect to the phase angle $\phi_t = 2\pi f_{\text{osc}} \frac{t}{f_c}$, while $_t$ is the sample number, f_c is

Table 2: Sensor and data aquisition card specifications

Load cell		
Sunrise		SRI M3714B
Axis		6
Resistance	[Ω]	350
Forces net	[N]	[800, 800, 1600]
Moment net	[Nm]	[44, 44, 44]
Prot. class		IP68
Data acquisition card		
Labjack		T7
Sample rate	[Hz]	1000
Discretization	[bit]	16

Table 3: Surface tracking measurment setup

Distance	D	[m]	1.07
Apparent Distance	D'	[m]	1.15
Pixel size	px_{size}	[m]	$2.4{\cdot}10^{-4}$
Dist. Proj./Camera	D_{PC}	[m]	0.36
App.Dist. Proj./Camera	D'_{PC}	[m]	0.28

the capturing frequency:

$$\alpha_t = \arctan\left(\frac{\sin\phi_t}{2+\cos\phi_t}\right) \tag{6}$$

During the experiment the hydrodynamic forces and moments, the volume flow rate, the temperature and the angle position of the foil are recorded with a data acquisition card (DAC) of 16 bit discretization rate and a sample rate of 1 kHz for each channel. The position is measured by the encoder of the servo drive. It features 8192 pulses per turn. This position feedback signal is later used for the method evaluation.

A six-axes load cell (SRI M3714B, see Tab.2) is installed fully submerged in between the drive shaft and the hydrofoil (see Fig.6). A detailed description and uncertainty considerations regarding the force measurements are given in [7].

In parallel to the DAC measurement the pattern for the surface tracking is projected on the surface with an EPSON EH-TW7300 projector. The lower surface of the structure is captured with a high speed camera at 4 kHz sample rate f_c (see Tab.3&4 for specifications). The synchronization of the data provided by the DAC and the high-speed recording is achieved with a trigger signal which starts the camera recording and is captured

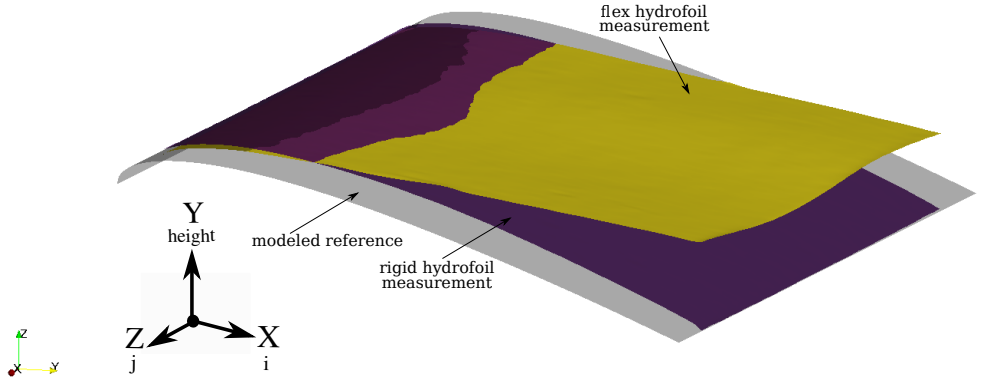

Figure 7: Surface measurement of the rigid (dark violet), the flexible hydrofoil (orange) and the artificial reference surfaces (grey and black) while the latter surface is overlaid by the first. For convenience regarding the presentation the shape is turned upside down, that the surface appears to be the upper side of the profile.

Table 4: High speed camera specifications

Phantom V2511		
Resolution	[px×px]	1280×800
Pixel size	[μm]	28
CMOS area	[mm×mm]	35.8×22.4
Color depth	[bit]	12
Focus	[mm]	105
Acquisition rate (max)	[fps]	25,000
Acquisition rate (exp)	[fps]	4,000
Exposure time (exp)	[μs]	60
Total frames		16500
Total acq. time	[s]	4.125

with dedicated channel of the DAC.

The composite hydrofoil is built of a rigid aluminum part at its first quarter chord followed by a carbon fiber plate of thickness 0.3 mm along the chord till the trailing edge. The profile is manufactured by casting with a white-pigmented two-component silicon polymer which provides the foil shape (see Fig.1(left)).

The natural frequencies of the hydrofoils were investigated experimentally[1] by a vibration testing method and are shown in Tab. 5. The hydro-

[1]The frequencies were taken from a student's report: Laddey, C.: *Untersuchung der Eigenfrequenzen hydrodynamischer Profile*, 2019, University of Applied Science Magdeburg

Table 5: Natural frequencies of the Hydrofoils

Hydrofoil		first	second
Flexible without sensor	[Hz]	53.3	162.35
Flexible with sensor	[Hz]	56.15	149.54
Rigid without sensor	[Hz]	254,5	300
Rigid with sensor	[Hz]	98.47	129.8

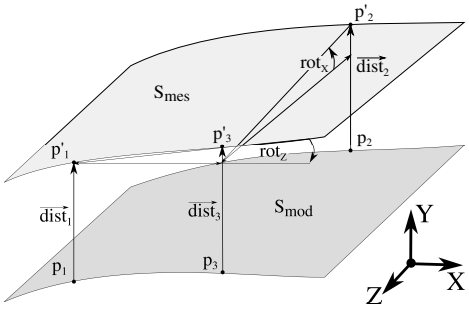

Figure 8: Surface tracking calibration: The calibration of the measuremnts is performed by three points for each sample. The calibration vector (containing $dist_1$, rot_X and rot_Z) is then averaged over the time to achieve a minimal error for the whole set.

Table 6: Material specifications

Aluminum alloy		EN	AW-7075
Young's Modulus	E	[Pa]	$72 \cdot 10^9$
Density	ρ	[kg/m^3]	2800
Tensile strength	$R_{p0.2}$	[Pa]	$450 \cdot 10^6$
Carbon Fibre			cg-tec.de
Young's Modulus	E	[Pa]	$52.7 \cdot 10^9$
Density	ρ	[kg/m^3]	1600
Fibre Orientation		[°]	0/90
Silicone			Wacker
Elastosil M4600			
Young's Modulus	E	[Pa]	$6.4 \cdot 10^5$
Density	ρ	[kg/m^3]	1100
Tensile strength		[Pa]	$7 \cdot 10^6$

foils mounted on the sensor were excited with a hammer strike. The free vibrations of the clamped structure were captured with a Laser Interferometer. The material characteristics are shown in Tab.6 [2].

The chord length of the hydrofoil C=0.066 m and the inlet flow speed of the water channel u_{ch}=3 m/s result in a blade based Reynolds number of $2 \cdot 10^5$.

The surface measurement is mapped to a pixel grid of size 276×600 for each frame.

The high speed camera is able to store 16500 frames which leads to a recording time of 4.125 s. During this time, the hydrofoil will perform 15 oscillations.

4 Calibration

The calibration and subsequent uncertainty considerations of the method are based on a video set of the rigid reference profile. This reference is compared to a modeled surface of the hydrofoil which performs an oscillation according to the position feedback of the drive system (see Sec.3). The calibration is necessary due to imprecisions during the installation. Aberrations in the angle in between camera and projector to the investigated surface, as well as the distance will impact the results.

[2]The mechanical properties for the silicone polymer are taken from a student's report: Laddey, C.: *Protokoll zum Zugversuch des Werkstoff Wacker Elastosil M4600*, 2018, University of Applied Science Magdeburg

Table 7: SFT calibration matrix

	X	Y	Z
Translation [m]	0	0.00106	0.015
Rotation [°]	0.014	0	-0.045

According to the differences in between the acquisition rate of the position feedback and the high speed recording each fourth frame of the high speed video was evaluated. The deformations of the rigid hydrofoil can be considered negligible.

The modeled hydrofoil surface is built using Eq.7, an expression describing a four digit NACA hydrodynamic profile contour [8]. The shape is calculated for a relative thickness τ=0.18 (the foil thickness in percent of the chord length/100) for a discrete number of points corresponding to the number of pixels in the X-axis. The resulting curve is rotated in accordance to the position feedback of the drive at quarter chord, scaled and finally extruded in Z-direction.

$$y = \frac{\tau}{0.20} \cdot (0.2969\sqrt{x_{\text{ad}}} - 0.126 x_{\text{ad}} - 0.3516 x_{\text{ad}}^2 + 0.2843 x_{\text{ad}}^3 - 0.1015 x_{\text{ad}}^4) \quad (7)$$

with x_{ad} the relative chord position, $x_{\text{ad}} = 0$ and $x_{\text{ad}} = 1$ corresponding respectively to the leading and trailing edges. A calibration algorithm was implemented as a utility (see *sft_cal.py* in [6]). The algorithm converts the calculated heights from the pixel based grid to the physical profile length in X- and Z directions ($n_X \times n_Z$). 100 pixels were cropped on both sides in the Z-axis of the profile to remove reflection noise from the wall of the test section of the channel (see Fig.6 for coordinates). The measured surface S_{mes} is centered in this axis with respect to the modeled surface S_{mod} (see Fig.7). As a consequence of the projection of both surfaces in a rectangular grid (see Fig.5), only three degrees of freedom remain unknown for a surface fit (see Fig.8). By the assumption that the differences of the shape of the surfaces are small, one translation vector and two rotation angles are sufficient to calculate the gap in Y direction between the two (similar) surfaces. This can be conducted with three points. The calibration vector is shown in Tab.7. The values for the rotation of 0.014° and -0.045° are negligible. The height shift is determined to be 1.06 mm. The position in the Y-axis depends also on the luminosity of the projection which unfortunately suffers from a flicker with 60 Hz frequency. The height for each take has

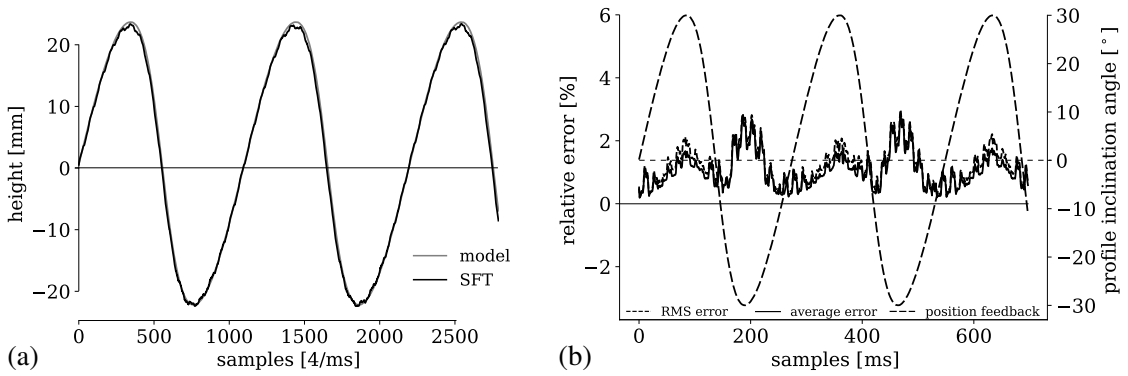

Figure 9: (a) Surface height over time, measurement compared to the model surface for one point ($h_{260,300,t}$) near the trailing edge for 2700 samples after calibration. (b) Relative error over time for the surface tracking measurement, compared to the model surface for one point ($_{260,300}$) near the trailing edge for 700 samples. The error is set in relation to the foil motion with Eq.9. The corresponding inclination angle (from position feedback of the drive) is plotted in the same diagram to display the influence of the profile inclination to the error.

to be adjusted once, which can be done by a known reference point, e.g. the height of any one point at quarter chord (where no deformation occurs) at zero inclination angle.
Fig.9a displays the height at a point situated near the trailing edge in the mid position of the surface ($h_{260,300,t}$). Generally the measurement method delivers accurate results. However, the deviations increase significantly for high inclination angles. This is due to a general drawback of the method as the measurement of a motion parallel to the zero plane is not feasible. This share of the motion increases with rising angle of inclination of the foil. These deviations are discussed and analyzed in detail in the following section.

5 Validation

The modeled surface created from the position feedback and the measurement of the rigid hydrofoil are compared in order to validate the method. The differences in height between the model $h_{\mathrm{mod}_{i,j,t}}$ and the measurement $h_{\mathrm{mes}_{i,j,t}}$ over a set of frames are evaluated using Eq.8. The validation is performed with the help of a postprocessing class (see *SFT_post.py* in [6]). In a first step, the temporal error δh_t at the point $h_{i,j} = h_{260,300}$ near the trailing edge at $i = 260$ is estimated.

This is followed by an evaluation of the spatial error $\delta h_{i,j}$ for an arbitrary frame in the time line $_t$. Here the calculation is evaluated for all pixels of the surface:

$$\delta h_{i,j,t} = h_{\mathrm{mes}_{i,j,t}} - h_{\mathrm{mod}_{i,j,t}} \tag{8}$$

Table 8: Error determination:
The error was calculated for the whole matrix exept 20px at the matrix borders. The method is prone to strong abbrevations there.

absolute error		
average error	[m]	0.00066
RMS error	[m]	0.00077
error relative to the motion range Eq.(9)		
relative average error	[%]	1.06
relative RMS error	[%]	1.23

The result is a three dimensional error matrix of size 276×600 with a depth of the evaluated set. Subsequently the error relative to the motion is calculated with respect to the amplitudes of the surface heights:

$$\delta h_{\mathrm{rel}_{i,j,t}} = \frac{\delta h_{i,j,t}}{\max\limits_{i,j,t}(h_{\mathrm{mod}}) - \min\limits_{i,j,t}(h_{\mathrm{mod}})} \tag{9}$$

The relative error is shown in Fig.9. The influence of the inclination angle is significant, as well as the impact of a flicker of 60 Hz from the projector, which can also be seen in the video recordings. It was decided to keep the data unfiltered rather than apply a low pass filter, in order to preserve the entire spectra of the motion as compared to the suppression of vibrations from the flicker which happens in the latter case, even though this suppression of vibrations further attenuates the error. The

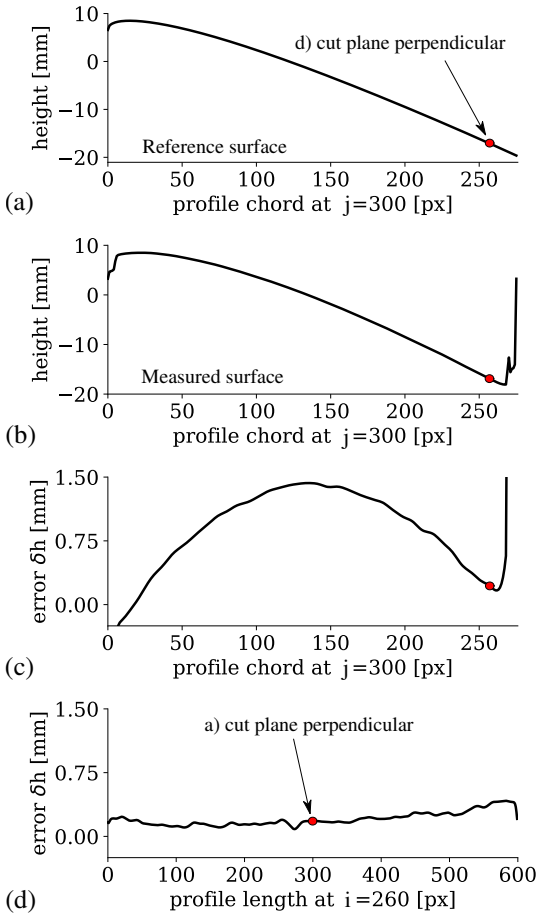

Figure 10: (From top to down) Modeled surface (a) measured surface of the inclined hydrofoil (b) and a measurement error to the reference surface for an arbitrary frame (t=223). The maximum chord wise error is found in the middle of the profile with around 1.4 mm (c) The maximum absolute error in the profile length is less the 0.4 mm (d). The inclination angle for this instant of time α=28°

.

method provides highest accuracy for low angles of inclination with a relative error magnitude less than 1%. The mean error was evaluated for all pixels of the surface, except the first 20 pixels at each border. The maximal foil motion (see Eq.9) was used as the reference for the relative error. The higher deviations occurring at high inclination angles of up to 3% lead to an average relative error of 1.06% over an entire oscillation period, which corresponds to an absolute value of 0.66 mm. The spatial error is shown for a cut section of the frame t=223, in the middle of the Z-axis $\delta h_{i,300,223}$ and subsequently for a slice of the X-axis near the trailing edge $\delta h_{260,j,223}$ (see Fig.10). The obvious aberrations on the hydrofoil borders become visible in particular for the chord wise cut. The shape of the error profile with its maximum of about 1.4 mm in the middle of the chord is in accordance to the errors reported by Maurel et al [12]. A treatment of the position shift (see Eq.3) may further reduce these deviations if necessary. In the Z-axis the error remains at an almost constant level except at the borders. Tab.8 summarizes the method accuracy for the case at hand. It has to be considered that the accuracy depends significantly on the constraints of the experiment. A higher accuracy can be achieved for smaller height differences and higher spatial resolution.

6 Results and analysis

In this part, some results and the first analyzes carried out using the measured fields are presented (in the physical space, and in the spectral space). It demonstrates the advantages of the proposed method.

6.1 Surface tracking and hydrodynamic forces

Fig.7 displays the two surfaces of the rigid and the flexible structure along with the analytical reference from Eq.7 imported to *Paraview*. A good agreement with the modeled reference can be found for the rigid hydrofoil measurement, both surfaces overlay with negligible error, in particular at the rear region of the structure. The bending of the flexible surface is also visualized, the non-deformable first quarter of the flexible structure fits in with the rigid one with good agreement. The flexible three quarters of the chord at the rear of the structure are deformed as a result of the hydrodynamic forces. The maximal height difference

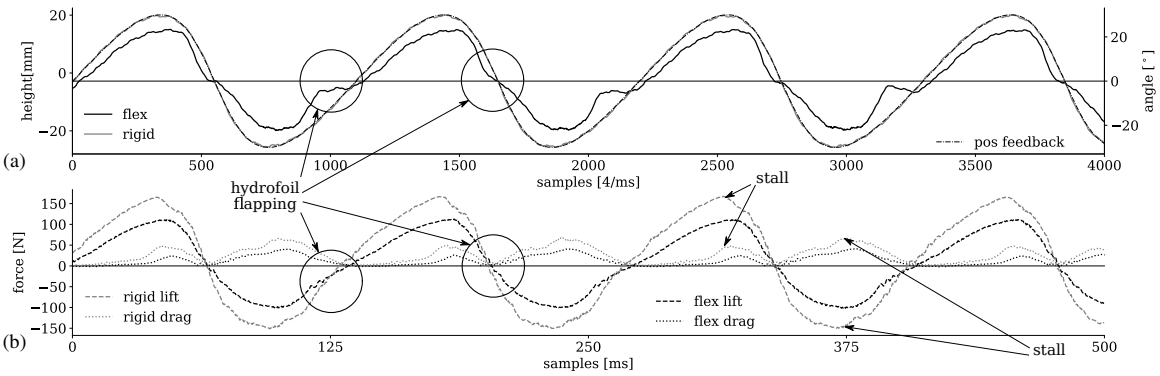

Figure 11: (a) Heights (left axis of ordinate), retrieved from measurement for rigid (light grey) and flexible hydrofoil (black) surface at 97% of the chord, compared to the position feedback (dashed-dot, black, right axis of ordinate) for 1 s with 4 kHz sample rate. The position feedback curve is almost congruent with the height curve of the rigid foil. (b) Corresponding lift (dashed) and drag (dotted) forces for the rigid (light grey) and the flexible hydrofoil (black) for 1 s with 1 kHz temporal resolution.

is about 14 mm compared to the rigid hydrofoil. These high deformations account for up to 20% of the chord length during the oscillations (see Fig. 11&12).

A "flapping" of the profile's trailing edge occurs periodically with stronger preference for the slower motion (direction of increasing α) starting at -20°. The faster pitch motion towards negative α features a less distinct flapping motion (starting at 20°), which can in consequence be assumed to be dependent on the pitch speed. It is supposed to be related to a flow separation and vortex shedding. For a full understanding of the mechanism, the knowledge of the flow field is necessary, which could be investigated with PIV measurements.

The hydrodynamic forces (see Fig.11b) captured from the load cell show decreased lift and drag for the flexible foil. No stall point is found for the flexible foil. A significant difference can be found for the drag force trajectory that features lower amplitudes and slope for the flexible hydrofoil compared to the rigid one. The influence of flexible blades on the thrust force in a vertical-axis water turbine was discussed in [7]. It was shown that a reduced drag even with a reduction in the lift force have clear benefits. The improvements from flexible blades concern turbine lifetime and thrust efficiency. In the subsequent section a spectral analysis was performed in order to describe the different FSI characteristics of the rigid and the flexible structures.

6.2 Spectral analysis

A spectral data analysis on the complete deformation field of the surfaces is performed. As a first step, reference data based on the theoretical motion law is generated.

Considering the oscillation imposed on the hydrofoil (Eq.6), the expression of the phase angle ($\phi_t = 2\pi f_{\text{osc}} \frac{t}{f_c}$) and the position of the pitch $p_{\text{pos}} = 0.25 \cdot C$, it is possible to express the surface of the hydrofoil as a function of time $\frac{t}{f_c}$ (t is the position index in the time line of a recording).
First, the chord position is defined without hydrofoil inclination

$$x_i = \frac{iC}{N_x} - p_{\text{pos}} \cdot C \tag{10}$$

with N_x equal to the number of pixels of the measurement; $N_x = 276$. Next, according to Eq.7 with $x_{\text{ad}} = \frac{iC}{N_x}$ the y_i position and subsequently the local height without inclination angle between surface and the horizon, $\alpha_{0,i} = \arctan\left(\frac{y_i}{x_i+\epsilon}\right)$ are calculated.
Finally, considering the re-projection on the grid as explained in Fig.5, the theoretical position of the surface according to the time can be easily determined:

$$h_{i,j,t,\text{analytic}} = \sqrt{x_i^2 + y_i^2} \cdot \sin\left(\alpha_t + \alpha_{0,i}\right) \cdot \text{sign}(x_i + \epsilon) \tag{11}$$

Please note that in order to avoid a division by zero (for the arctangent function) and for the sign equal to 0 a regularization has to be performed; $\epsilon = 1e-15$. The spectra are calculated with the following expressions :

$$H_{i,j,m} = \frac{1}{f_c} \sum_{t=0}^{N_t-1} h_{i,j,t} \cdot e^{-2\pi t \frac{mt}{N_t}} \tag{12}$$

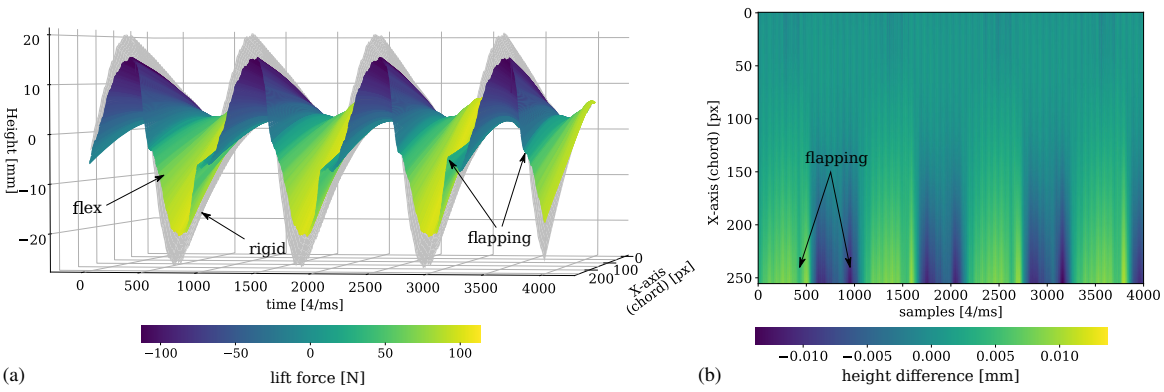

Figure 12: (a) Three dimensional representation of the trajectory of a slice of rigid (grey) and the flexible hydrofoil (colored by it's instantaneous lift force). The surface is shown for a chord wise slice of the hydrofoil at is middle position. These slices are plotted over time with 4 samples/ms. (b) Representation of the difference between the rigid and the flexible surface for a chord wise slice in the middle of the surfaces over time.

$$H_{j,q,m} = \frac{1}{f_c}\frac{1}{px_{\text{size}}}\sum_{i=0}^{N_x-1}\cdot\sum_{t=0}^{N_t-1} h_{i,j,t}\cdot e^{-2\pi\iota\left(\frac{mt}{N_t}+\frac{qi}{N_x}\right)} \tag{13}$$

where $H_{i,j,m}$ is the single-point spectrum value at point $(_{i,j})$ for a frequency equal to $\frac{m f_c}{N_t}$. $H_{j,q,m}$ is the two dimensional spectrum for a slice at transversal position j for a chord wave number (in X-axis) equal to $\frac{q}{N_x \cdot px_{\text{size}}}$ and the frequency equal to $\frac{m f_c}{N_t}$.

The number of temporal snapshots N_t is chosen to be exactly proportional to the period of the forced oscillation. It avoids the use of a temporal weighting window. Concerning the two dimensional processing (Eq. 13) a hanning spatial weighting window is applied to the $h_{i,j,t}$ signal (in order to limit the spectrum leakage due to the implicit rectangular window [16]).
Similar expressions are used in the transversal spectra (replacing i by j, and N_x by N_y) in the Eq. 12&13.

Then, in a second step, a spectral analysis of the rigid hydrofoil surface is performed from the measured data, $h_{i,j,t}$. In direct comparison, the measurement technique presented shows good accordance to the analytical results, as the spectra of the deformation fields for the rigid hydrofoil and the artificial data are in good agreement. Finally, a spectral analysis on the case of the flexible hydrofoil is conducted. The results are shown in Fig.14-16.

The two dimensional spectra show no resonance in the spatial modes. Indeed, although the spectra of the flexible hydrofoil case are more intense (which can be explained by a response of the flexible structure), there is no specific trace for any wave number k in X or Z direction. On the other hand, the two dimensional spectra of the flexible hydrofoil show very clearly the attenuation of some frequencies by comparison to the rigid case; e.g. the frequency $f = 18.3$ Hz.

6.3 Forced oscillation and fluid-structure interaction

The flow field and the hydrodynamic forces are dominated by the forced oscillation. The spectral analysis allows to distinguish between the primary effects of the motion and the secondary effects from the fluid-structure interaction. Fig.17 shows the spectra for lift force, position feedback and surface tracking for a point near the trailing edge. The left plot is for the rigid foil. A good accordance of position feedback and surface tracking can be observed, which is expected. The lift force shows, for the lower frequencies, good accordance to the position feedback as well. A much broader spectrum is found in particular in a frequency band of 20 to 40 Hz. Here, significant peaks become visible but encounter no structural response. For frequencies above 50 Hz the signal becomes noisy.

For the flexible foil, only the position feedback features a smooth spectrum with few peaks in accordance to the rigid hydrofoil case. As opposed to the rigid foil, the lift force and the surface in this case show good accordance for frequencies up to 50 Hz. Here, as in the previous setup, the

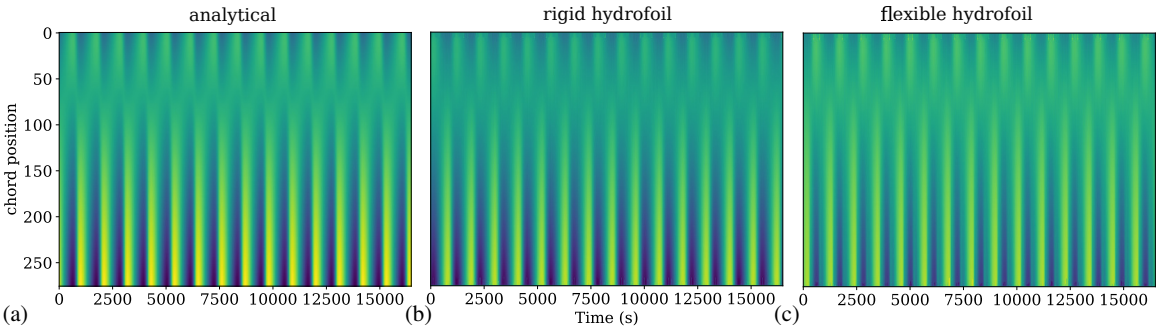

Figure 13: Plot of the height at the middle transversal position over the time. (a) analytical heights from Eq.10&11; (b) measured heights of the rigid hydrofoil; (c) measured heights of the flexible hydrofoil with the technique presented

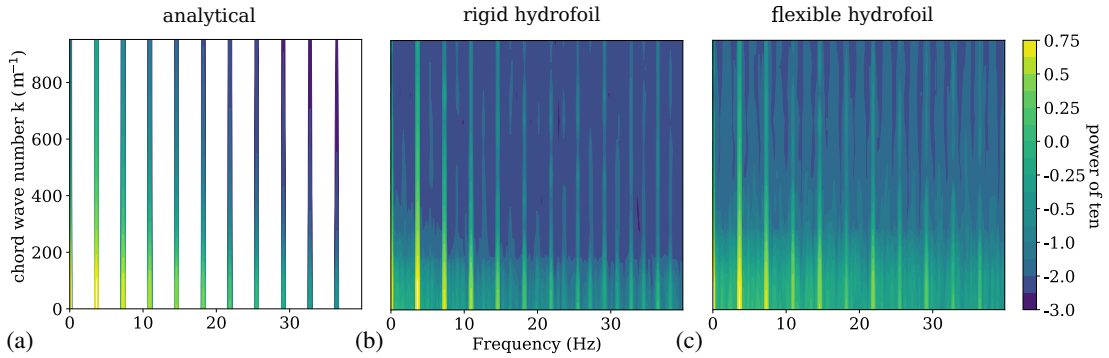

Figure 14: Longitudinal (X-axis) two dimensional spectra, wave number over frequency, of the data shown in Fig.13. (a) analytical; (b) rigid hydrofoil; (c) flexible hydrofoil

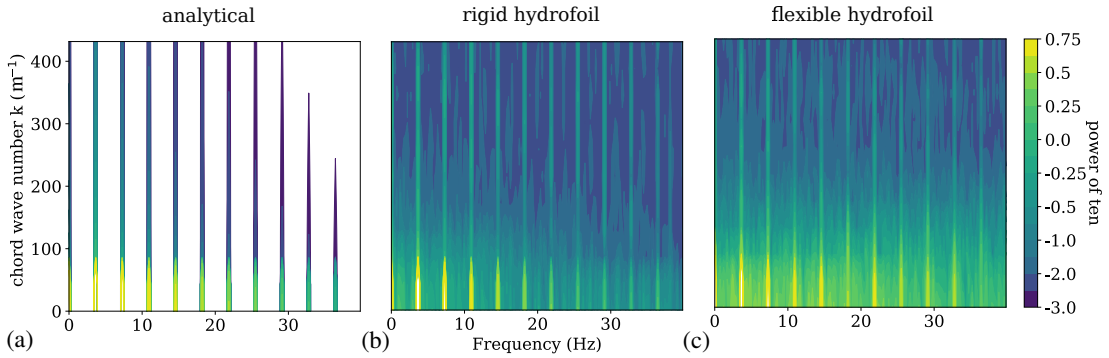

Figure 15: Transversal (Z-axis) two dimensional spectrum, wave number over frequency, of the height at a near trailing edge position. (a) analytical case; (b) rigid hydrofoil; (c) flexible hydrofoil

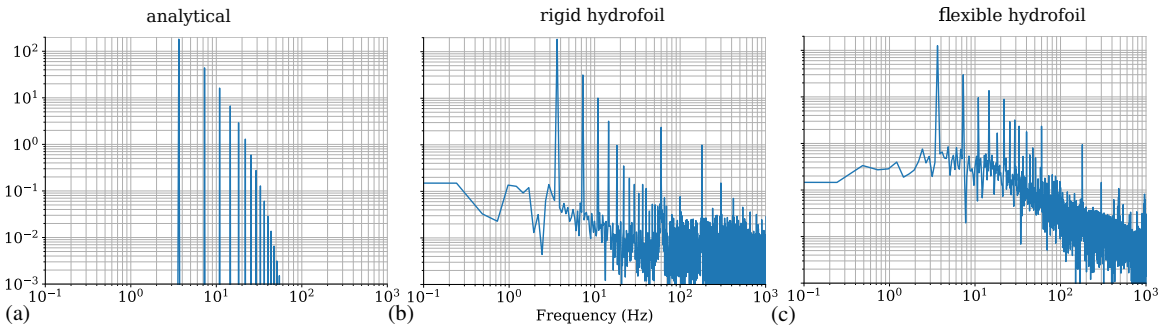

Figure 16: Point spectrum of the height at a position near trailing edge. (a) analytical case; (b) rigid hydrofoil; (c) flexible hydrofoil.

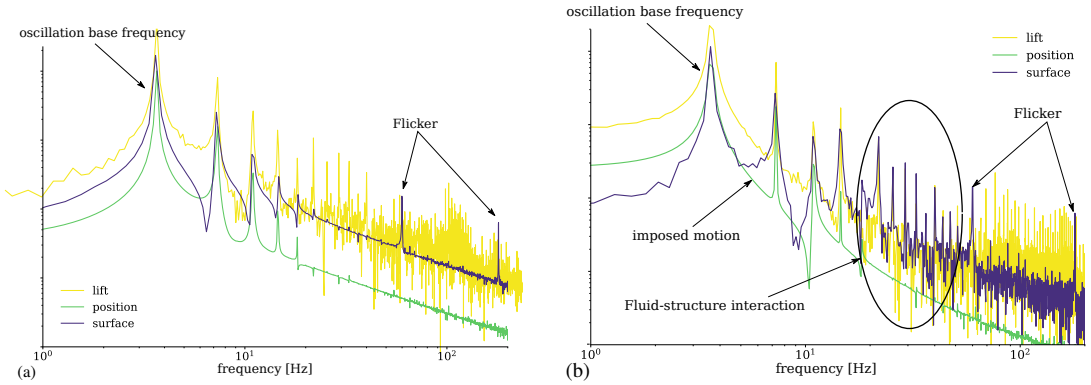

Figure 17: Point spectra of the lift force, the position feedback and the surface near the trailing edge. The spectra of the surface were shifted to a common level for better visibility. (a) rigid hydrofoil; (b) flexible hydrofoil.

signal becomes noisy afterwards. However in the bandwidth from 20 to 40 Hz, significant FSI phenomenon become visible as the surface frequencies correspond perfectly to the lift force without excitation from the forced motion.

In both cases, the flicker frequencies (60 and 180 Hz) are clearly visible.

7 Conclusions

In this study, a structured-light based measurement methodology was applied on a FSI case, consisting of a hyper-flexible hydrofoil set under a non-sinusoidal pitch motion in a closed water channel.

The method and implementation are accurately detailed, which will allow to adapt and utilize it in custom FSI applications. The source code of the implementation is published under CeCILL-B and freely available.

Moreover the method shows high accuracy with about 1% average relative error in relation to the foil motion. The averaged absolute error was found to be 0.66 mm. The advantages of the method are its simplicity and its modest hardware requirements (a projector and a high-speed camera), compared to other common techniques in FSI that provide the instantaneous deformation field, like Stereoscopic Digital-Image-Correlation. Moreover, the simultaneous measurement of hydrodynamic loads and structural deformation with a time resolved instantaneous deformation field is achieved, which provides insights into the FSI with a reasonable effort.

In the displayed application, which models the performance of a vertical-axis hydroturbine with flexible blades, the deformation measurements linked to the corresponding instantaneous hydrodynamic forces show a deformation of up to 20% of the chord length. These deformations are accompanied by a reduction in lift along with a strong reduction of the drag, and are advantageous as the lifetime and turbine thrust are improved.

The measurement of most of the surface, with high temporal and spatial resolution, allows to

investigate instantaneous structural response by a two-dimensional spectrum analysis, and provides deeper knowledge than a point-wise time-averaged investigation with Laser interferometer. This from particular interest for a comparison of hydrofoils with different stiffness which is the scope of future work.

For now, the spectral analysis allows to distinguish between the primary, direct influence of the imposed motion and the secondary FSI with the hydrodynamic excitation of the structure visible at higher spectra.

Work is ongoing to develop a combination of the presented methodology with instantaneous flow field measurements carried out with PIV. This would enable to continue the investigation of the FSI on flexible turbine blades, with the aim of linking of those higher spectra to mechanisms such as boundary layer separation or vortex shedding.

It is also envisaged to post-process the two dimensional instantaneous data by more advanced methods like Proper Orthogonal Decomposition or Linear Stochastic Estimation. At least this allows filtering of the data, but ideally it will allow a decomposition of the global phenomenon into a set of small simple phenomenons. The link between these with another field (lift for example) could then be studied.

Acknowledgements

The corresponding author is grateful for the funding of his thesis by a scholarship of the Rosa-Luxemburg-Stiftung Berlin, by the Wachstumskern Flussstrom Plus research project (03WKC02B), financed by the German Federal Ministry of Education and Research, and the funding of German-French-University Saarbrücken.
The authors thank the Unité Mixte de Service Grenoble - Alpes Recherche Infrastructure et Calcul Intensif et de Données (UMS-GRICAD) for their services. Carsten Laddey and Christian-Thoralf Weber (University of Applied Sciences Magdeburg) are thanked for their help with obtaining material specifications and the natural frequencies of the hydrofoils. The support of Pierre Augier (LEGI), Nicolas Mordant (LEGI), Shokoofeh Abbaszadeh (OvGU), Olivier Cleynen (OvGU), Michael Haarman (CATLAB, Berlin), Michel Riondet (LEGI), Jean-Marc Barnoud (LEGI) and Christian Kisow (OvGU) is gratefully acknowledged.

References

[1] Astolfi, J., Lelong, A., Bot, P., Marchand, J.B.: Experimental analysis of hydroelastic response of flexible hydrofoils. In: 5th High Performance Yacht Design Conference, Auckland (2015)

[2] Augier, P., Bonamy, C.: Fluidimage (2019). URL `https://bitbucket.org/fluiddyn/fluidimage`

[3] Augier, P., Mohanan, V., Bonamy, C.: Fluiddyn: a python open-source framework for research and teaching in fluid dynamics by simulations, experiments and data processing. Journal of Open Research Software (2019)

[4] Ducoin, A., Astolfi, J.A., Sigrist, J.F.: An experimental analysis of fluid structure interaction on a flexible hydrofoil in various flow regimes including cavitating flow. European Journal of Mechanics - B/Fluids **36**, 63 – 74 (2012). DOI https://doi.org/10.1016/j.euromechflu.2012.03.009

[5] Hassaini, R., Mordant, N.: Confinement effects on gravity-capillary wave turbulence. Physical Review Fluids **3** (2018). DOI 10.1103/PhysRevFluids.3.094805

[6] Hoerner, S.: Sft utilities repository (2019). URL `https://bitbucket.org/sthoerner/sft_utilities`

[7] Hoerner, S., Abbaszadeh, S., Maître, T., Cleynen, O., Thévenin, D.: Characteristics of the fluid–structure interaction within darrieus water turbines with highly flexible blades. Journal of Fluids and Structures **88C**, 13–30 (2019). DOI 10.1016/j.jfluidstructs.2019.04.011

[8] Jacaobs, E., Ward, K., Pinkerton, R.: Report 460 - the characteristics of 78 related airfoil sections from tests in the variable-density wind tunnel. Tech. rep., NACA National Advisory Commitee for Aeronautics (1933). URL `ntrs.nasa.gov/archive/nasa/casi.ntrs.nasa.gov/19930091108.pdf`

[9] Li, H., Zhang, K., Waldman, R.M., Hu, H.: Quantification of dynamic droplet impact onto a solid surface by using a digital image projection technique. In: 55th AIAA Aerospace Sciences Meeting. American Institute of Aeronautics and Astronautics (2017). DOI doi:10.2514/6.2017-0942

[10] Lin, H., Jian Gao, G.Z., Chen, X., He, Y., Liu, Y.: Review and comparison of high-dynamic range three-dimensional shape measurement techniques. Journal of Sensors p. 11 (2017). DOI https://doi.org/10.1155/2017/9576850

[11] MacPhee, D.W., Beyene, A.: Fluid-structure Interaction analysis of a morphing vertical axis wind turbine. Journal of Fluid and Structures **60**, 143–159 (2016). DOI 10.1016/j.jfluidstructs.2015.10.010

[12] Maurel, A., Cobelli, P., Pagneux, V., Petitjeans, P.: Experimental and theoretical inspection of the phase-to-height relation in fourier transform profilometry. Applied Optics **48**(2), 380–392 (2009)

[13] Naik, T., Longmire, E.K., Mantell, S.C.: Dynamic response of a cantilever in liquid near a solid wall. Sensors and Actuators A: Physical **102**(3), 240 – 254 (2003). DOI https://doi.org/10.1016/S0924-4247(02)00398-9

[14] Nakata, T., Liu, H.: A fluid–structure interaction model of insect flight with flexible wings. Journal of Computational Physics **231**(4), 1822 – 1847 (2012). DOI https://doi.org/10.1016/j.jcp.2011.11.005

[15] Pärssinen, T., Eloranta, H., Saarenrinne, P.: Experimental investigation of material effects on free vibration of a splitter plate. Experiments in Fluids **42**(3), 349–362 (2007). DOI 10.1007/s00348-006-0240-8

[16] Prabhu, K.: Window Functions and Their Applications in Signal Processing, 1st edition edn. CRC Press (2014). DOI 10.1201/9781315216386

[17] Rojratsirikul, P., Wang, Z., Gursul, I.: Unsteady fluid–structure interactions of membrane airfoils at low reynolds numbers. Experiments in Fluids **46**(5), 859 (2009). DOI 10.1007/s00348-009-0623-8

[18] Takeda, M., Ina, H., Kobayashi, S.: Fourier-transform method of fringe-pattern analysis for computer-based topography and interferometry. Journal of the Optical Society of America **72**(1), 156–160 (1982)

[19] Tregidgo, L., Wang, Z., Gursul, I.: Unsteady fluid–structure interactions of a pitching membrane wing. Aerospace Science and Technology **28**(1), 79 – 90 (2013). DOI https://doi.org/10.1016/j.ast.2012.10.006

[20] Van der Jeught, S., Dirckx, J.J.: Real-time structured light profilometry: a review. Optics and Lasers in Engineering **87**, 18 – 31 (2016). DOI https://doi.org/10.1016/j.optlaseng.2016.01.011. Digital optical & Imaging methods in structural mechanics

[21] Voss, S., Saalfeld, S., Hoffmann, T., Beuing, O., Weigand, S., Jachau, K., Preim, B., Thévenin, D., Janiga, G., Berg, P.: Fluid-structure simulations of a ruptured intracranial aneurysm: Constant versus patient-specific wall thickness. Computational and Mathematical Methods in Medicine **2016**, 1–8 (2016). DOI 10.1155/2016/9854539

[22] Zhang, S.: High-resolution, High-speed 3-D Dynamically Deformable Shape Measurement Using Digital Fringe Projection Techniques, chap. 2. IntechOpen, Rijeka (2010). DOI 10.5772/8720